Direct numerical simulation of internally heated natural convection in a hemispherical geometry

Boshen Bian[1], Daniele Dovizio[2], Walter Villanueva[1,3]
[1]Division of Nuclear Power Safety, Royal Institute of Technology (KTH), Sweden
[2]Nuclear Research and Consultancy Group, The Netherlands
[3]Nuclear Futures Institute, Bangor University, United Kingdom

Highlights

1. A direct numerical simulation of an internally heated natural convection at Ra=1.6×10^{11} and Pr=0.5 is presented.
2. A simple pre-estimation of mesh requirements and post-check verification is implemented.
3. Typical turbulence quantities and the budgets of TKE and THF are generated and discussed.

Abstract

Internally heated (IH) natural convection can be found in nature, industrial processes, or during a severe accident in a light water reactor. In this accident scenario, the nuclear reactor core and some internal structures can melt down and relocate to the lower head of the reactor pressure vessel (RPV) and interact with the remaining coolant. Subsequent re-heating and re-melting under decay and oxidation heat creates a transition from a debris bed to a molten pool. The molten pool, which can involve more than hundred tons of dangerously superheated oxidic and metallic liquids, imposes thermo-mechanical loads on the vessel wall that can lead to a thermal and/or structural failure of the vessel and subsequent release of radioactive materials to the reactor pit, and can possibly make its way to the environment. This study uses Direct Numerical Simulation (DNS) to investigate homogeneous IH molten pool convection in a hemispherical domain using Nek5000, an open-source spectral element code. With a Rayleigh number of 1.6×10^{11}, the highest reached through DNS in this confined hemispherical geometry, and a Prandtl number of 0.5, which corresponds to a prototypic corium, the study provides detailed information on the thermo-fluid behaviour. The results show a turbulent flow with three distinct regions, consistent with the general flow observations from the BALI experiments. The study also presents detailed information on turbulence, such as turbulent kinetic energy (TKE), turbulent heat flux (THF), and temperature variance. Additionally, the study provides 3D heat flux distributions along the boundaries. The heat fluxes along the top boundary fluctuate due to the turbulent eddies in the vicinity, while along the curved boundary the heat fluxes increase nonlinearly from the bottom to the top.

Keywords:

internally heated natural convection, molten pool, DNS, turbulence

1. Introduction

The thermo-fluid behaviour of molten pools across wide-ranging orders of Rayleigh (Ra) and Prandtl (Pr) numbers is not yet fully understood and universal laws are still up for debate [1]. This phenomenon can be found in nature, e.g., the Earth's mantle convection and in industrial

processes or emerging technologies such as Gen-IV nuclear reactors with molten pools of salt or metal. In light water reactors (LWRs), a molten pool of heat-generating debris can form in the lower head of a reactor pressure vessel (RPV) during a severe accident progression. The melt consists of in-vessel components, especially reactor fuels which contain harmful radioactive elements. Because of the decay heat within the fuel material, the melt can eventually become a molten pool, usually referred to as corium in severe accident analysis. To retain the radioactive corium inside the RPV, one mitigation strategy is to utilize an external cooling system based on the criteria of In-Vessel Melt Retention (IVMR) safety design [1]. However, one prerequisite of the success of IVMR is that the heat flux imposed along the inner wall of the RPV is not supposed to exceed the Critical Heat Flux (CHF). When the heat flux goes beyond the CHF limit, it can lead to a rapid increase in temperature, reduced heat transfer, and potential damage or failure of the RPV. Therefore, it is important to ensure that the heat flux remains below the CHF to maintain structural integrity of the RPV. Therefore, it is crucial to investigate the thermo-fluid behaviour of the corium to predict the heat flux distribution. The configuration of the corium can vary from a 2-layer or 3-layer stratification to a homogenous molten pool. In this study, we only consider the situation of a homogenous molten pool in a hemispherical geometry which simulates the lower head of the RPV.

The thermo-fluid behaviour of the corium is characterized as an internally heated (IH) natural convection phenomenon, because of the absence of an external force and the presence of a decay heat source [3]. Different from forced convection flow, natural convection flow is mainly driven by the buoyancy force caused by the temperature difference, and controlled by the Rayleigh number, Ra, and the Prandtl number, Pr. If such a temperature difference is induced by the boundary conditions, the natural convection is known as Rayleigh–Bénard (RB) convection. If it is induced by an internal heat source, the natural convection is called IH convection [4]. RB convection has been studied tremendously for a large variety of both Rayleigh and Prandtl numbers. Grossmann and Lohse formulated a regime map of the assessment of flow and heat transfer property of the RB convection with respect to Ra and Pr [5]. In each regime, the scaling of Nusselt number and Reynolds number in relation to Ra and Pr are obtained. Regarding IH natural convection, Goluskin has done a series of theoretical analyses. He proposed to normalise the governing equation of the IH convection with the Oberbeck-Boussinesq assumption and divide the IH convection into three different categories based on the boundary condition [4]. The one with a Dirichlet thermal boundary is called IH1 which is the same case in this study. In analogy with the Grossmann and Lohse's theory of RB convection, Goluskin proposed a regime division theory and a scaling relationship in IH convection [6]. He also conducted a Direct Numerical Simulation (DNS) of IH convection in a box and quantified the heat transfer asymmetry in the gravity direction within different Rayleigh numbers (10^6-5×10^{10}) and Prandtl numbers (0.01-10) [7]. Compared with Goluskin's work, IH convection studies with a corium pool involve a more complex geometry and a higher Ra.

During the last three decades, huge amount of research on molten pool simulation have been carried out both experimentally and numerically [8]. The BALI experiments [9] were conducted by CEA in a two-dimensional 1/4 circular slicing geometry with a thickness of 15

cm, whose Ra was up to 10^{17} and the corium simulant was water. The results showed that high Rayleigh numbers would generate strong turbulent flow in the IH natural convection. A general observation of the flow pattern and temperature distribution in the experiments is shown in Figure 1. The domain of the test section could be divided into three regions. An intensive turbulent zone with a homogenous temperature appeared in the upper part. Below it, flow motion was suppressed but goes up with much reduced intensity. Further, a descending flow along the curved boundary was observed. In addition to the BALI experiments, the COPO series of experiments, the SIMECO experiments [12] and the COPRA experiments [10] [11] were also performed in two-dimensional slice facilities. Another group of molten pool experiments was performed in hemispherical facilities, for example, the ACOPO experiments [13] and the LIVE experiments [14]. A summary of these experiments is presented in Table 1.
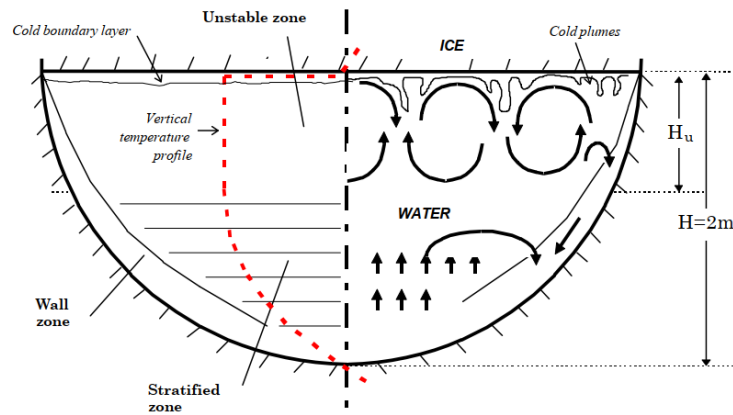

Figure 1 General flow observation in BALI experiment [9].

Table 1: Summary of experiments (not exhaustive)

Experiment	Geometry	Simulant material	Rayleigh number	Prandtl number
COPO-1 [10]	Semi-elliptical slice	$ZnSO_4$-H_2O solution	10^{14}-10^{16}	≈ 3
COPO-2 [11]	-Semi-elliptical slice -Semicircular slice	Corium: $ZnSO_4$-H_2O solution Metal layer: Distilled water	10^{14}-10^{16}	≈ 3
BALI [9]	1/4 circular slice	Salt Water	10^{13}-10^{17}	≈ 7
SIMECO [12]	Semicircular slice	$NaNO_3$-KNO_3	10^{12}-10^{15}	≈ 13
LIVE [14]	Hemisphere	$NaNO_3$-KNO_3	10^{13}	8.1-10.4
ACOPO [13]	Hemisphere	Water	10^{12}-10^{16}	≈ 7
COPRA [15]	1/4 circular slice	$NaNO_3$-KNO_3	Up to 10^{17}	8.1-10.4

However, designing and conducting corium pool experiments requires a large amount of investment in financial and human resources. Apart from that, there exist additional limitations and difficulties e.g., the limitation of the Prandtl number of the simulant. In the prototypic corium pool, the Pr is around 0.5 [16] and it is challenging to find the proper simulant with similar Pr in the experiment. In fact, in all the experiments mentioned above, water or salt solution was used, resulting in Pr larger than 3. Therefore, the development of methodologies to simulate IH molten pool convection has been gaining much interest in recent years. Taking advantage of the flexibility and low financial cost, the numerical analysis of the molten pool convection problem became popular. However, the analysis of complicated configuration molten pool still relies heavily on experiments. In terms of simulation accuracy, one of the biggest remaining challenges in the computational aspect of this field is the highly intensive turbulence of the IH natural convection at high Rayleigh number. Different turbulence models have been implemented to simulate the corium pool, for example, Reynolds Averaged Navier Stokes (RANS), Large Eddy Simulation (LES), and Direct Numerical Simulation (DNS), in that order of least-to-most expensive and least-to-most accurate. As for the RANS models, it was reported by Nourgaliev et al. that standard low Reynolds k-ε models failed to predict the near-wall turbulence region in IH convection at high Rayleigh number because of the strong anisotropic behavior adjacent to the walls [17]. Shams developed the algebraic heat flux model AHFM-NRG+ by adding a non-linear Reynolds stress model and an advanced turbulent heat flux model to the low Reynolds k-ε model, and it showed a good agreement against the BALI experimental results [18]. Based on the same model, Whang et al. combined it with SST, and analyzed the effect of the Prandtl number on the molten pool convection [19]. An LES with Mason-Derbyshire Smagorinsky sub-grid model was compared with the k-ε model on numerically simulating the BALI experiment by Fukasawa et al. [20], and it was shown that LES was better to predict the turbulent behavior in the molten pool. Zhang et al. also evaluated the Wall-Modeled LES (WMLES) method by comparing it with three corium experiments: BALI, LIVE and COPRA experiments [21].

However, both RANS and LES models must incorporate assumption models on turbulence, while a DNS method describes turbulence without any assumption, and provide the most accurate result. The strongest limitation for the utilization of DNS is the computational cost, because the mesh resolution of a DNS case is generally extremely large. The mesh size must be smaller than the smallest dissipation scale in the bulk. In addition, it should also meet the requirement in the boundary layer. Nevertheless, given the huge development of computational resources, DNS is becoming more popular in turbulence simulations nowadays, especially in cases with simple geometries [22,23]. Furthermore, DNS can also provide more comprehensive information of flow motion and heat transfer. Various turbulent quantities can be calculated in DNS, such as the Reynolds stresses, $\overline{u_i' u_j'}$, turbulent heat fluxes, $\overline{u_i' \theta'}$ (THF), turbulent kinetic energies (TKE), k, which could be directly used in the assessment of RANS models. Moreover, the budgets of TKE and THF, as well as the temperature variance can be obtained, which can help both qualify and quantify the turbulence. In this work, a DNS is conducted on a homogeneous oxidic molten pool in a hemispherical geometry. The Rayleigh number in the molten pool is 1.6×10^{11} given the current limitation in computational resources. The main objectives are (i) to study the thermal-hydraulic property of a highly intensive turbulent IH

convection in a molten pool in the most accurate way, and (ii) to provide the most comprehensive information on the turbulent flow.

2. Mathematical modelling

2.1 Governing equations and computational domain

When modeling IH natural convection, the Oberbeck-Boussinesq approximation is commonly incorporated into the incompressible Navier-Stokes equation. It assumes that the density variation of the fluid depends only on the temperature change, such that

$$\frac{\rho - \rho_*}{\rho_*} = -\beta(\Theta - \Theta_*) \tag{1}$$

Where $\rho \, [\frac{kg}{m^3}]$ is the density of the fluid, $\Theta \, [K]$ is the temperature, $\beta \, [\frac{1}{K}]$ is the coefficient of thermal expansion. ρ_* and Θ_* are reference density and temperature respectively. Therefore, the governing equations of the mass, momentum, and energy for an internally heated natural convection flow are [4]:

$$\nabla \cdot \boldsymbol{u} = 0$$

$$\frac{\partial \boldsymbol{u}}{\partial t} + \boldsymbol{u} \cdot \nabla \boldsymbol{u} = -\frac{1}{\rho_*} \nabla p + \nu \, \nabla^2 \boldsymbol{u} + g\beta\Theta\vec{z} \tag{2}$$

$$\frac{\partial \Theta}{\partial t} + \boldsymbol{u} \cdot \nabla \Theta = k\nabla^2\Theta + \frac{Q}{\rho c_p}$$

where $\boldsymbol{u} = (u, v, w)[\frac{m}{s}]$, Θ and $p \, [Pa]$ denotes the velocity, temperature and pressure field, respectively. In addition, $\nu \, [\frac{m}{s^2}]$ is the kinematic viscosity, $c_p [\frac{J}{kg \cdot K}]$ is the heat capacity, $k[\frac{W}{m \cdot K}]$ is the thermal conductivity and $g[\frac{m}{s^2}]$ is the gravitational acceleration in the opposite of the vertical direction $\vec{z}$. The last term on the right-hand side of the momentum equation represents the buoyancy force induced by the density difference, which is along the vertical direction, $\vec{z}$. In the energy equation, $Q[\frac{W}{m^3}]$, is the volumetric heat source which is homogenous in the computational domain. To generalize the problem, the equations can be normalized using the characteristic length $l \, [m]$, a time scale $\frac{l^2}{\alpha} \, [s]$ and a temperature scale $\Delta = \frac{l^2 Q}{\alpha \rho c_p} \, [K]$, where $\alpha[\frac{m^2}{s}]$ is the thermal diffusivity[4], which yield the following equations

$$\nabla \cdot \boldsymbol{u} = 0$$

$$\frac{\partial \boldsymbol{u}}{\partial t} + \boldsymbol{u} \cdot \nabla \boldsymbol{u} = -\nabla p + Pr \, \nabla^2 \boldsymbol{u} + RaPr\Theta\vec{z} \tag{3}$$

$$\frac{\partial \Theta}{\partial t} + \boldsymbol{u} \cdot \nabla \Theta = \nabla^2\Theta + 1$$

5

where the velocity, temperature and pressure field are normalized. So $\boldsymbol{u}$, Θ and p now represent the non-dimensional fields from this point onwards. As a result of the normalization, two non-dimensional numbers, Rayleigh and Prandtl numbers are obtained in the equation, whose expressions are $Ra = \frac{g\beta l^3 \Delta}{\alpha v}$ and $Pr = \frac{v}{\alpha}$. The Rayleigh number indicates the ratio of the fluid inertial force to the viscous force, which can be treated as the primary control number of the IH natural convection. If it is large, the effect of the buoyancy force is strong and the flow is more intense. The Prandtl number is a material dependent parameter, representing the ratio of the momentum diffusion to heat diffusion. The computational model used in this work has been verified using a calculation performed by Goluskin and van der Poel [4] on a simplified internally heated 3D box with excellent agreement (see [3] for details).

In this study, a 3D hemispherical cavity is considered to model the lower head of the RPV, as shown in Figure 2. The gravity acceleration, g, acts opposite to the vertical direction $\vec{z}$. The domain is filled with an incompressible fluid which is bounded by two non-slip walls. To simulate the IH natural convection, a uniform heat source is set inside the domain, and an isothermal condition is specified at the boundaries. The summary of the case conditions is reported in Table 2
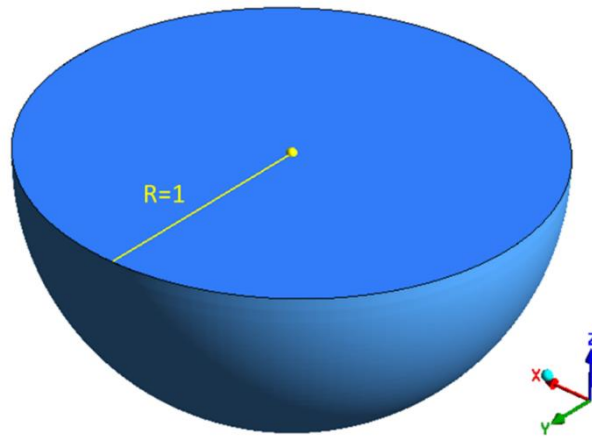

Figure 2 Computational Domain.

Table 2 Case conditions

Thermal Boundary	$\Theta = 0$
Velocity Boundary	No-slip wall
Rayleigh Number	1.6×10^{11}
Prandtl Number	0.5

2.2 Turbulence quantities

As mentioned previously, the flow in the IH molten pool is fully turbulent because of the high Rayleigh number. To quantify the turbulence, one can always perform Reynolds decomposition of the governing equations i.e., a field variable can be divided into a mean value and a turbulent fluctuation value. For example, $d = \bar{d} + d'$, where $\bar{d}$ is the temporal average of d and d' is the instant fluctuation with the property of $\overline{d'} = 0$. In this way, the time-averaged field of the IH natural convection flow can be described as

$$\frac{\partial \overline{u_i}}{\partial x_i} = 0$$

$$\frac{\partial \overline{u_i}}{\partial t} + \frac{\partial}{\partial x_j}(\overline{u_j u_i}) = -\frac{\partial \bar{p}}{\partial x_i} + Pr\frac{\partial}{\partial x_j}(\frac{\partial \overline{u_i}}{\partial x_j}) - \frac{\partial \left(\overline{u_i' u_j'}\right)}{\partial x_j} + RaPr\overline{\Theta}\vec{z} \qquad (4)$$

$$\frac{\partial \overline{\Theta}}{\partial t} + \frac{\partial}{\partial x_i}(\overline{u_i \Theta}) = \frac{\partial}{\partial x_i}(\frac{\partial \overline{\Theta}}{\partial x_i}) - \frac{\partial \left(\overline{u_i' \Theta'}\right)}{\partial x_i}$$

In the momentum equation, an additional term, $\nabla\overline{u_i' u_j'}$ appears. $\overline{u_i' u_j'}$ is called Reynolds stress, and it denotes the impact from the turbulent fluctuation field to the mean flow field. Similarly, $\nabla\overline{u_i' \Theta'}$ is added in the energy equation. $\overline{u_i' \Theta'}$ is called turbulent heat flux, and it denotes the impact from the turbulence to the mean temperature field.

Another turbulent quantity of interest is the turbulent kinetic energy (TKE), k which can indicate the intensity of turbulence. The definition is $k = \frac{1}{2}\left(\overline{u'u'} + \overline{v'v'} + \overline{w'w'}\right)$. Based on the definition, one can derive the following normalized transport equation of the TKE in the IH natural convection

$$\frac{\partial k}{\partial t} + \overline{u}\cdot\nabla k = -\overline{u_j' u_i'}\frac{\partial \overline{u_j}}{\partial x_i} - Pr\overline{\left(\frac{\partial u_j'}{\partial x_i}\right)^2} + Ra\,Pr\,\overline{w'\Theta'} + \frac{\partial}{\partial x_i}\left(Pr\,\overline{u_j'\frac{\partial u_j'}{\partial x_i}} - \frac{1}{2}\overline{u_i' u_j' u_j'} - \frac{1}{\rho}\overline{u_i' p'}\right)$$

$$(5)$$

On the left, the first term is the time derivative of the TKE, and the second term is the spatial advection. One the right-hand side, the first one is the production term of the shear force, the second term is the viscous dissipation, the third term is the production term of the buoyancy force, and the last term is the spatial redistribution caused by viscous, turbulent and pressure effects, respectively. Compared to the TKE budget of the flow without buoyancy force, the buoyancy production, $Ra\,Pr\,\overline{w'\Theta'}$, is an additional term which balances the turbulent kinetic energy. It is proportional to the vertical component of the turbulent heat flux, $\overline{w'\Theta'}$.

The THF is modelled using the temperature gradient in some RANS models. In the AHFM model, there is a developed algebraic formula to model the turbulent heat flux. Therefore, we are also interested in the budget of the THF terms, especially the one in the vertical direction. The transport equation of the THF is shown in equation 6. On the left, the first term is the time derivative of the THF, and the second one is the advection term. One the right-hand side, there are the diffusion (consisting of viscous diffusion, turbulent diffusion, and pressure diffusion),

the shear production, the pressure temperature gradient (PTG), the dissipation and the buoyancy production terms, respectively. Notably, the buoyancy production term, which is proportional to the temperature variance $\overline{\Theta'\Theta'}$, only exists in the budget of the vertical THF, $\overline{w'\Theta'}$.

$$\frac{\partial \overline{u_i'\Theta'}}{\partial t} + \overline{u_j}\frac{\partial \overline{u_i'\Theta'}}{\partial x_j} = D_{u_i'\Theta'} + P_{u_i'\Theta'} + \Phi_{u_i'\Theta'} - \varepsilon_{u_i'\Theta'} + B_{u_i'\Theta'}\vec{z} \tag{6}$$

$$D_{u_i'\Theta'} = \frac{\partial}{\partial x_j}\left\{\overline{u_i'\frac{\partial \Theta'}{\partial x_j}} + \frac{1}{Pr}\overline{\Theta'\frac{\partial u_i'}{\partial x_j}}\right\} - \frac{\partial \overline{u_j'u_i'\Theta'}}{\partial x_j} - \frac{\partial \overline{p'\Theta'}}{\partial x_i}$$

$$P_{u_i'\Theta'} = -\overline{u_j'\Theta''}\frac{\partial \overline{u_i}}{\partial x_j} - \overline{u_i'u_j'}\frac{\partial \overline{\Theta'}}{\partial x_j}$$

$$\Phi_{u_i'\Theta'} = \overline{p'\frac{\partial \Theta'}{\partial x_i}}$$

$$\varepsilon_{u_i'\Theta'} = (1 + \frac{1}{Pr})\overline{\frac{\partial u_i'}{\partial x_j}\frac{\partial \Theta'}{\partial x_j}}$$

$$B_{u_i'\,\theta'} = Ra\,Pr\cdot\overline{\Theta'\Theta'}\vec{z}$$

3. Numerical treatment

3.1 Numerical scheme

The problem is solved using Nek5000, which is an open source CFD code with spatial discretization based on the Spectral Element Method (SEM) [24]. SEM can be treated as the combination of the Finite Element Method (FEM) and the Spectral Method (SM), which combines both the generality of the former and the accuracy of the latter [25]. With SEM, the computational domain is divided into elements, similar to FEM. In each SM element, the unknowns can be represented using a chosen function space and the weight on the collocation points in the element. In Nek5000, the Lagrange polynomials are selected as the base function and the Gauss-Legendre-Lobatto (GLL) points are selected as the collocation points. In this way, a relatively higher order accuracy can be achieved with a smaller number of elements, making it suitable for DNS calculations with simple geometries [26].

3.2 Meshing strategy

In generating the mesh for DNS simulations of turbulent flows, the smallest dissipation length scale needs to be taken care of, not only in the bulk, but also the small scales in the boundary layers. From this aspect, the boundary layer thickness should be identified first, then one can estimate the mesh size in both the bulk domain and the boundary layers based on the dissipation estimation. Based on the pre-estimation results, the mesh can be constructed. However, the mesh should also be post-verified using the simulation result of the dissipation length scale to

ensure that it satisfies the requirement of the DNS. The schematic of the meshing strategy in this DNS work includes three steps, as shown in Figure 3.
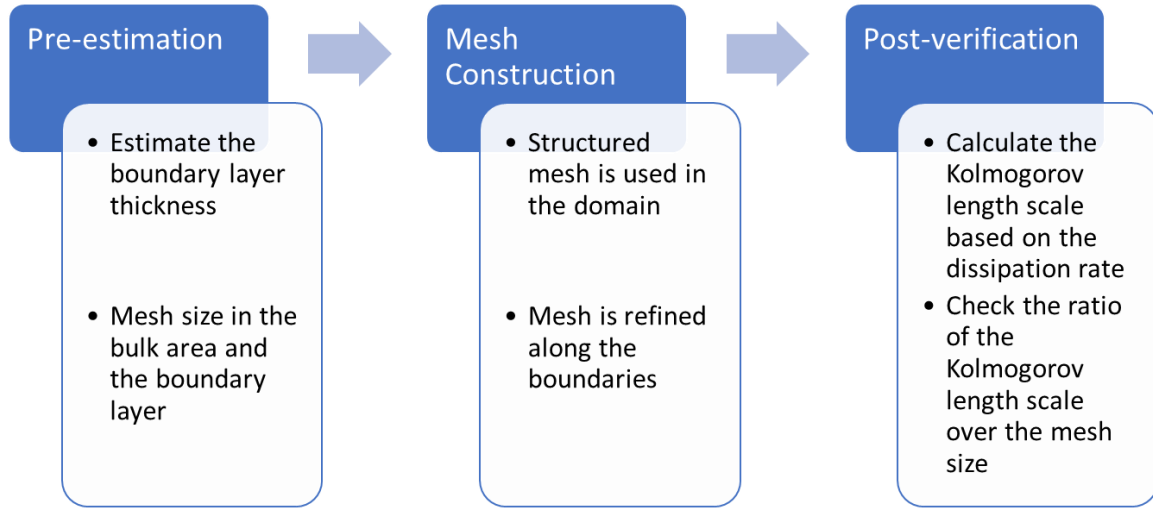
Pre-estimation
- Estimate the boundary layer thickness
- Mesh size in the bulk area and the boundary layer

Mesh Construction
- Structured mesh is used in the domain
- Mesh is refined along the boundaries

Post-verification
- Calculate the Kolmogorov length scale based on the dissipation rate
- Check the ratio of the Kolmogorov length scale over the mesh size

Figure 3 Workflow of the DNS mesh construction.

In the pre-estimation step, the first task relies on the identification of the boundary layer thickness in IH natural convection flow. Grossman and Lohse proposed a Ra-Pr phase-diagram method to estimate the boundary layer thickness in the natural convection in a wide range of Rayleigh and Prandtl numbers [5]. Similar to the forced convection flow, the kinetic boundary layer thickness and the thermal boundary layer thickness can be estimated using the Reynolds number, Re and the Nusselt number, Nu, and these two numbers can be estimated based on Ra and Pr of the flow, i.e. $Re = C_1 Ra^\alpha Pr^\beta$ and $Nu = C_2 Ra^\alpha Pr^\beta$. The power coefficients are determined according to the location of the Ra-Pr point on the diagram. In this way, the boundary layer thickness can be pre-calculated. After that, the mesh size within the boundary layer and the bulk flow can be calculated using Shishkina et al.'s formulas which are derived based on the dissipation analysis of the natural convection [27]. As mentioned, the computational domain consists of elements, and they are divided by the GLL grid points on the element edges according to the polynomial order. In this case, the distance between adjacent grid points must satisfy the mesh size requirement.

As a result, the total number of elements in the mesh is 764K. The mesh on the middle plane is shown in Figure 4, and it is shown that the mesh along the boundaries has been refined. The polynomial order of the element discretization is 7, which yields 391M grid points in the whole domain.
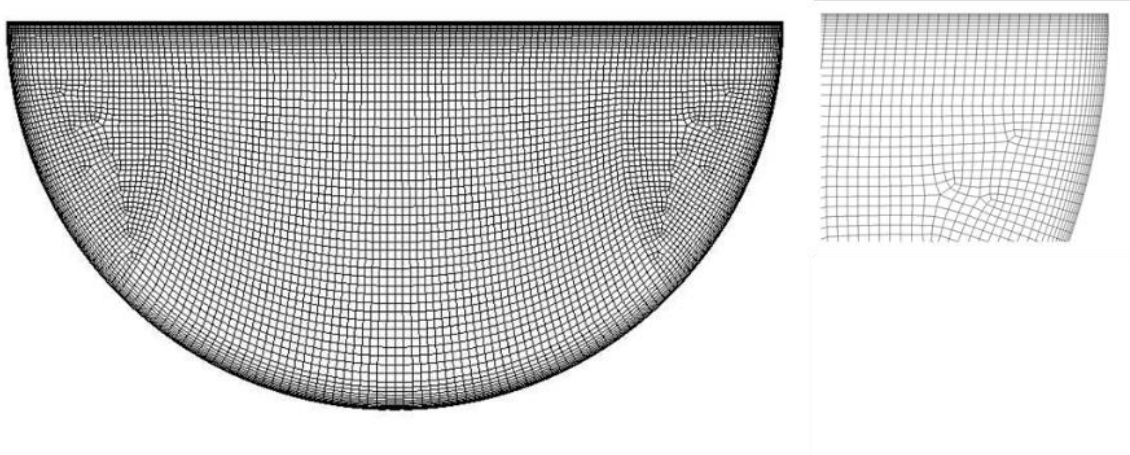
Figure 4 Overview of the element distribution on the XZ-middle slice of the domain, and the refined mesh near the boundary layers.

In the post-verification step, the mesh resolution is checked based on the dissipation distribution from the resulting DNS simulation. With the dissipation rate throughout the domain, one can calculate the Kolmogorov length scale. In this way, the mesh size can be compared with the Kolmogorov length scale using a ratio between them. In this work, the rotated spatial-average Kolmogorov length scale distribution on the vertical middle planes by averaging along the whole circumference of the 3D domain is presented based on the DNS simulation result (Figure 5). It is shown that in the upper part of the domain and along the curved boundary, the Kolmogorov length scale is smaller (red color in the figure), which means it requires higher mesh resolution in the corresponding areas. To check the ratio between the Kolmogorov length scale and the mesh size, we have looked through the ration over the plane. Figure 6 (b) gives a histogram of the ratio on each element over the slice, and all of them have been kept above 1, which means that the mesh size is smaller than the smallest dissipation rate.
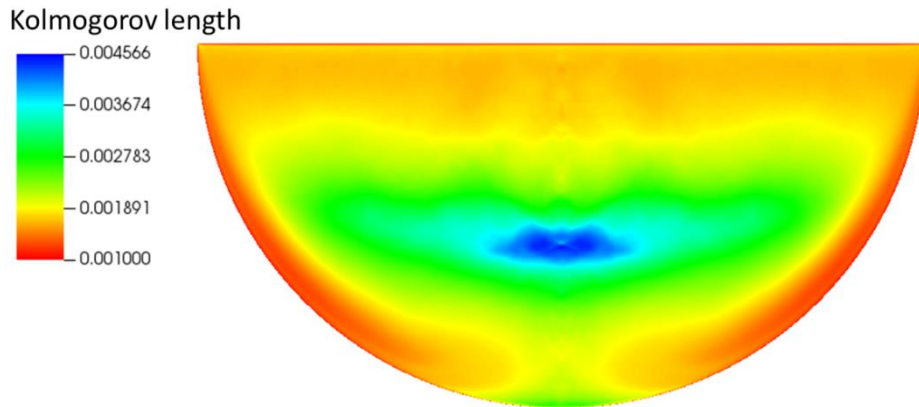
Figure 5 The spatial-average Kolmogorov length scale distribution of the domain generated from the DNS.
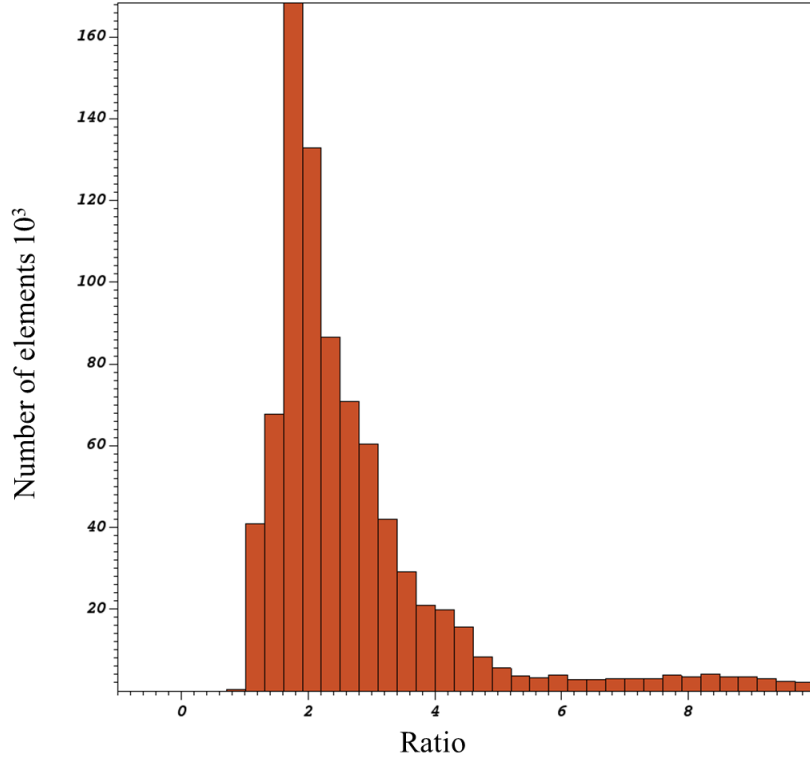
Figure 6 Ratio distribution between the Kolmogorov length and the mesh cell size.

The overall settings of the simulation are listed in Table 3. A quasi-steady state must be achieved in the simulation, which means that the balance of the competing terms or effects has been established. Due to convergence issues, the simulation starts from a small Rayleigh number, e.g., ~10^6. After that, the Ra is increased gradually until it reaches the target value of 1.6×10^{11}, which can provide a reasonable initial field for the actual simulation. Since then, it runs for a sufficient time to reach the quasi-steady state. Finally, time averaging quantities are calculated until the values converge to a small range i.e., 1%. This DNS work is conducted on the Beskow Cluster at the KTH PDC center with 2048 processor using around 4M core-hour computational time.

Table 3 Numerical Parameters of the DNS simulation in Nek5000

Element Number	764K
Number of quadrature Points	391M
Polynomial order	7
Target CFL	3.6
Maximum timestep	1×10^{-6}

4. Results and discussions

In this chapter, the DNS results of the IH natural convection at the quasi-steady state regime are presented. To facilitate the visualization of the simulation results, we have defined additional locations in the domain where post-processed data is captured, apart from the two boundary surfaces. As depicted in Figure 7(a), the XZ-middle plane (corresponding to an angle with respect to the x-axis: $r = 0°$) and the line between the centrals of the top and curved surface are referred to as the "middle slice" and "middle line" respectively in the following text. On the middle slice, the instantaneous velocity and temperature fields are presented, alongside mean quantities such as mean velocity, mean temperature, TKE, THF, and temperature variance. It is important to note that both temporal and spatial averaging are applied to the mean fields. More specifically, we have used 72 vertical slices equally distributed along the whole circumference of the 3D domain for spatial averaging, as shown in Figure 7(b). In Figure 7(c), we have included 50 horizontal planes along the vertical direction. On each plane, a quantity such as temperature can be averaged over the plane surface and plotted as vertical distributions. It is worth mentioning that all quantities presented in the following sections are dimensionless.

(a)

(b)

(c)
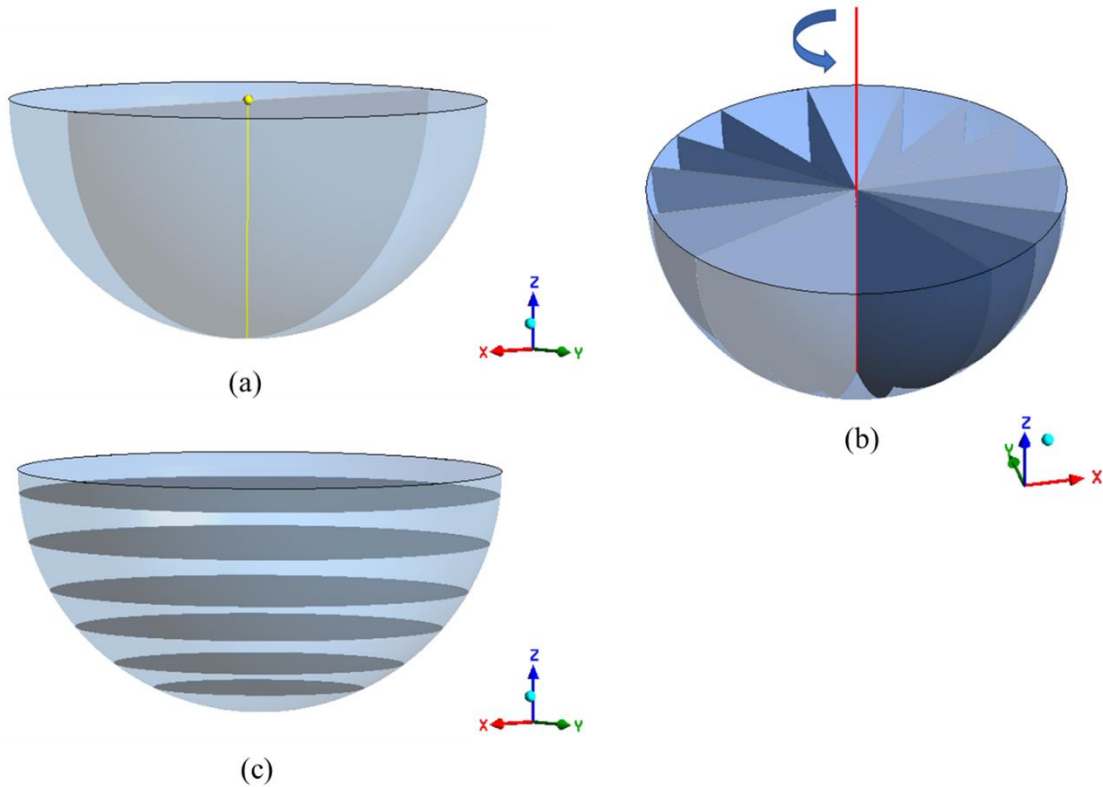
Figure 7 Locations in the domain to illustrate the results. (a) XZ middle plane and middle line. (b) 72 vertical equally distributed slices. (c) Multiple (50 in actuality) vertically distributed XY planes.

4.1 Velocity field

The instantaneous velocity distribution of the molten pool circulation at the quasi-steady state on the middle slice ($r = 0°$) is shown in Figure 8. Note that the turbulence is intense inside the domain, especially along the boundaries. Also, Figure 9 gives the instantaneous velocity distribution on four different vertical slices. Like the BALI experimental observations, the velocity field is divided into three zones: the upper mixing zone, the stagnation zone in the middle of the domain and the descending flow. The time-and-spatial-averaged velocity distribution is shown in Figure 10. The velocities in the descending flow are the largest through the domain. It can be observed that there are two large circulations inside the domain. The flow goes down along the curved boundaries and then goes up around the stagnation zone. After mixing in the upper zone, it will go towards the curved wall and then go down again.
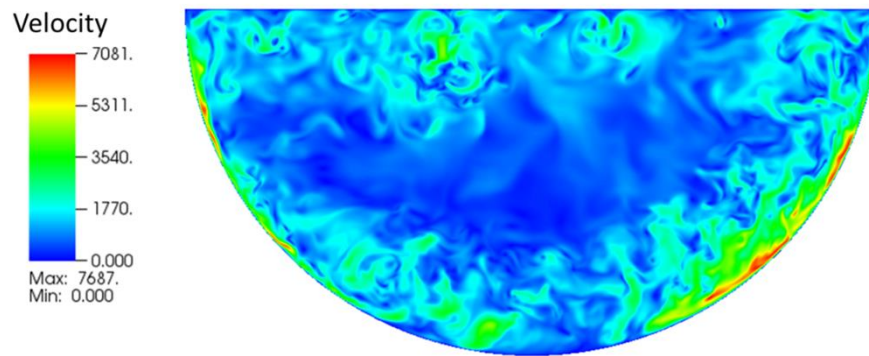
Figure 8 Instantaneous velocity magnitude distribution on the middle slice.
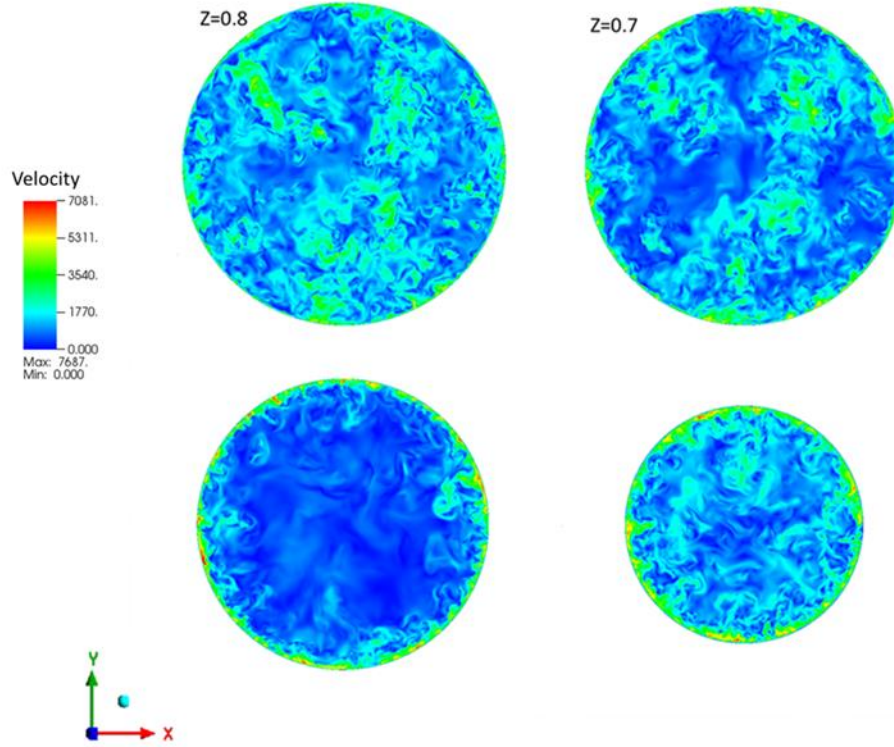
Figure 9 Instantaneous velocity magnitude distributions on the XY-slices with different vertical level.
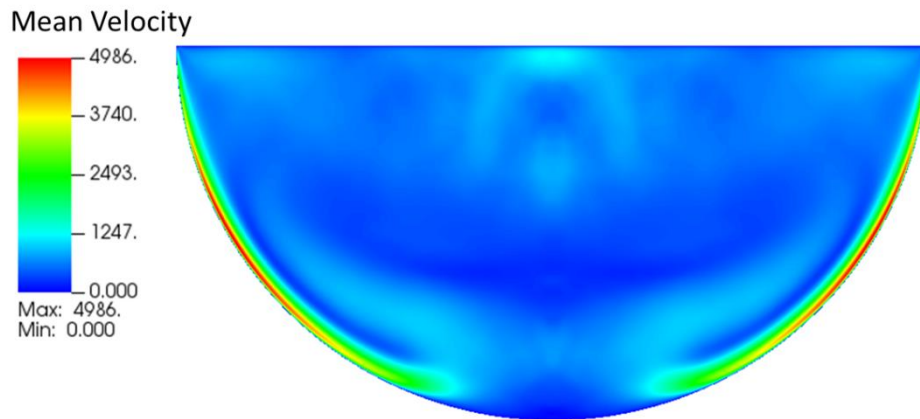

Figure 10 Averaged velocity magnitude distribution.

4.2 Temperature field

An instantaneous temperature distribution on the middle plane is shown in Figure 11. Because of the turbulent eddies in the upper zone, there are several evident cold plumes along the top boundary. There are also hot temperature plumes along with the descending flow. At the end of the descending flow and in the vicinity of the bottom, cold plumes are observed again due to turbulent eddies there. Figure 12 shows the space-and-time-averaged temperature distribution. We also plot the mean temperature profiles both along the middle line of the

14

domain and the averaged values on multiple vertical planes (Figure 13). In the upper zone, due to the mixing effect of the turbulence, the mean temperature from both profiles tends to be homogenous. In the lower part of the domain, the temperature calculated through the multiple vertical planes gradually decreases resembling a linear slope, while the values taken along the middle line present a concave behaviour around z=0.3. The averaged values on multiple vertical planes tend to be smoother because it takes the whole vertical plane into account, i.e., including the effects of the walls in the form of plumes penetrating in the bottom, as can be seen in Figure 12.

The temperature distribution is consistent with the three regions described in Figure 1. More specifically, the volumetric heat source generates thermal energy in the domain, while the two cold boundaries extract the energy out. The natural convection flow is mainly driven by the vertical buoyancy force which is caused by the temperature difference. In the upper zone, the cold boundary is on the top, so the flow is propelled by the buoyancy force. In the lower part of the domain, the cold boundary is at the bottom, so in contrast, the buoyancy force will suppress the flow motion. Due to the presence of the cold curved boundary, the flow near it will be cooled down and hence it then descends along the boundary because of the density difference. As for the vortices along the descending flow, they are mainly caused by the shear forces of the flow motion.
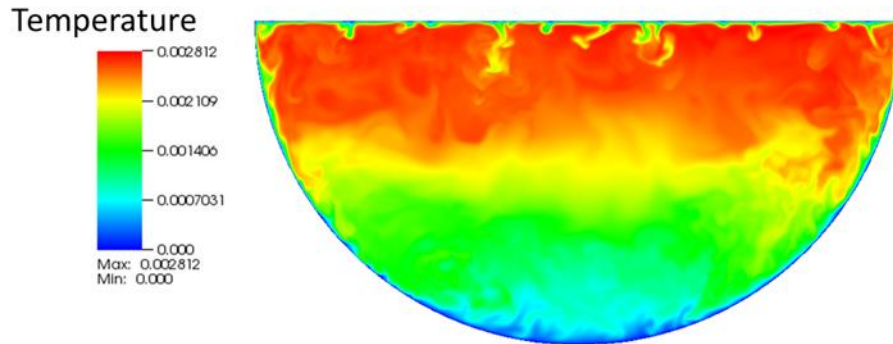

Figure 11 Instantaneous temperature distribution on the middle slice.
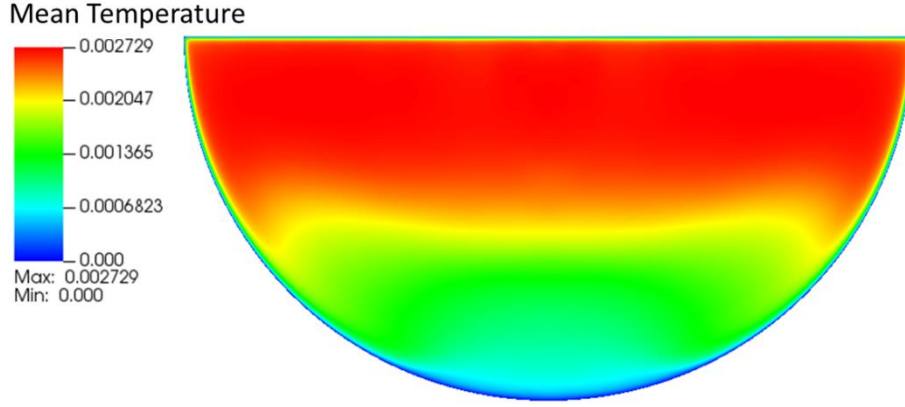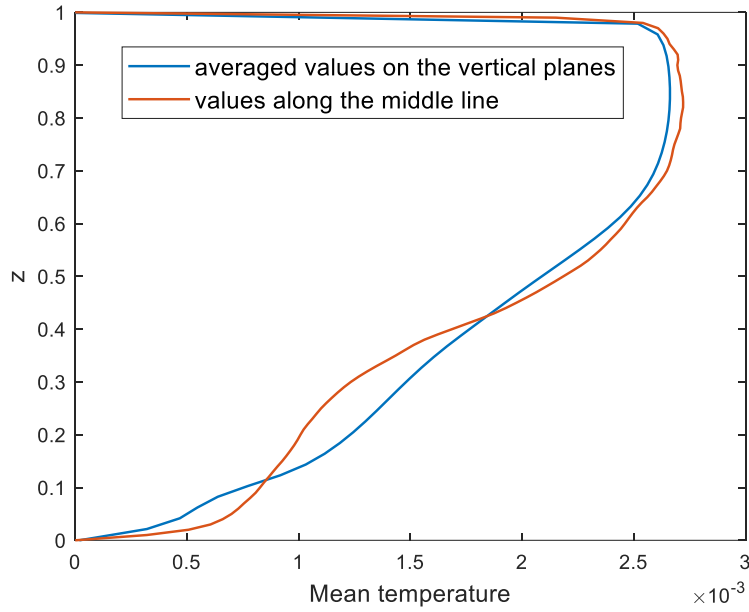
Figure 12 Averaged temperature distribution.

Figure 13 Averaged temperature profiles along the vertical direction.
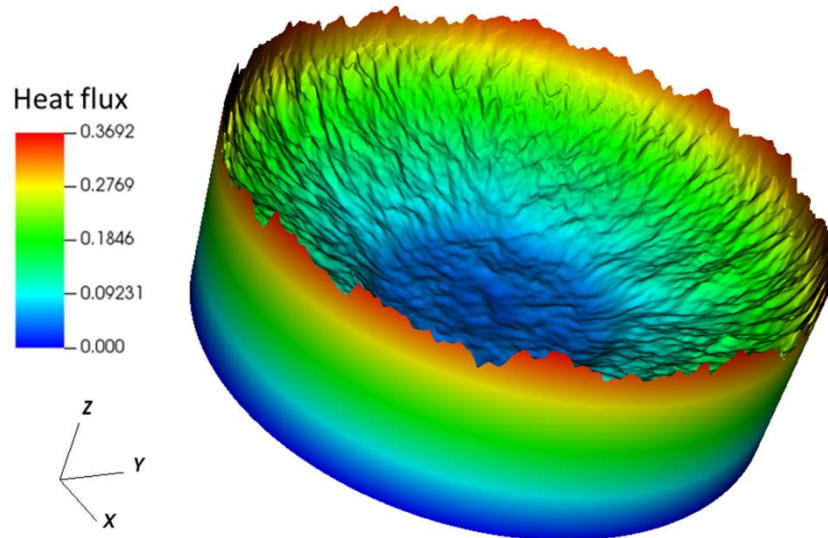
4.3 Heat flux

In the molten pool simulation, the heat flux along the boundaries is of great importance, because it directly influences the success of the IVMR mitigation strategy. In this work, we capture the time-averaged heat flux distribution at the top and the curved boundaries. Figure 14 presents the 3D plot of the time-averaged heat fluxes at the walls. The heat flux profile in Figure 14(a) shows that it is distributed unevenly because of the periodic turbulent eddies in the upper part of the domain. The peaks on the surface indicate the locations where the convection heat transfer is enhanced by the vortices. The 3D heat flux distribution on the curved wall is given in Figure 14(b), by projecting it on the top wall. From the center to the edge, the heat flux increases gradually. The uneven surface also reflects the effect of the turbulent eddies along the descending flow. Furthermore, we provide the 2D mean heat flux plot on the boundaries of 8 different 1/4 slices (see Figure 15 (a)) in Figure 15 (b). Each of the heat flux profiles has been spatially averaged on the boundary on 8 uniformly distributed 1/4 planes in

16

the domain. Due to turbulent eddies along the top wall (from the centre to the edge), the heat flux tends to fluctuate within a small range, having several peaks even after a long time-averaging. Along the curved boundary, the polar angle in the plot is measured from the bottom of the wall which means the angle is zero at the bottom. It shows that the heat flux increases as the polar angle increases, and it can be divided into three regimes according to the increasing rate. In the area near the bottom (0-20 degrees), the heat flux is almost constant and at the lowest value. This is because of the low turbulence near the bottom, which make the convection weak and homogenous. Then, in the middle (20-75 degrees) of the curved boundary, the effect of the descending flow becomes stronger. As a result, the effect of convective heat transfer increases gradually, which is reflected by the nearly linear increase in heat flux. In the upper part (75-90 degrees), the heat flux increases at a higher rate, due to the combination of the turbulent mixing caused by the top eddies and the descending flow, until reaching the maximum value, which is at the same level of the top boundary. The overall power split on the boundary surface is also calculated, which shows that 46% of the internally generated heat is released on the top wall and the remaining 54% goes out from the curved wall.

(a)

(b)

17
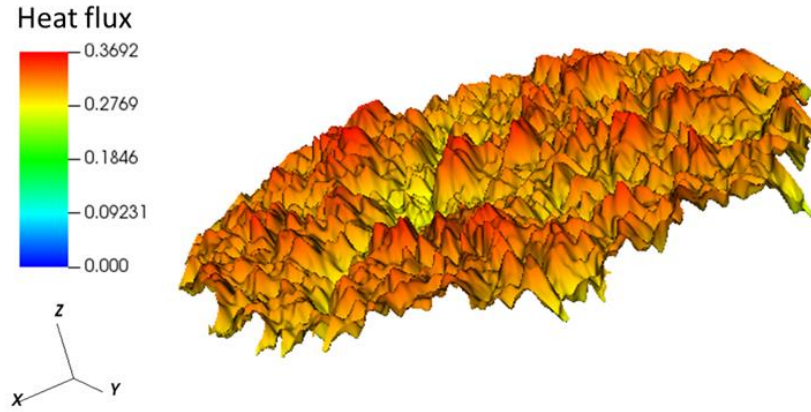
Figure 14 3D heat flux profile on the boundaries. (a) Heat flux of the top wall. (b) Projection of the heat flux of the curved wall on the top wall.
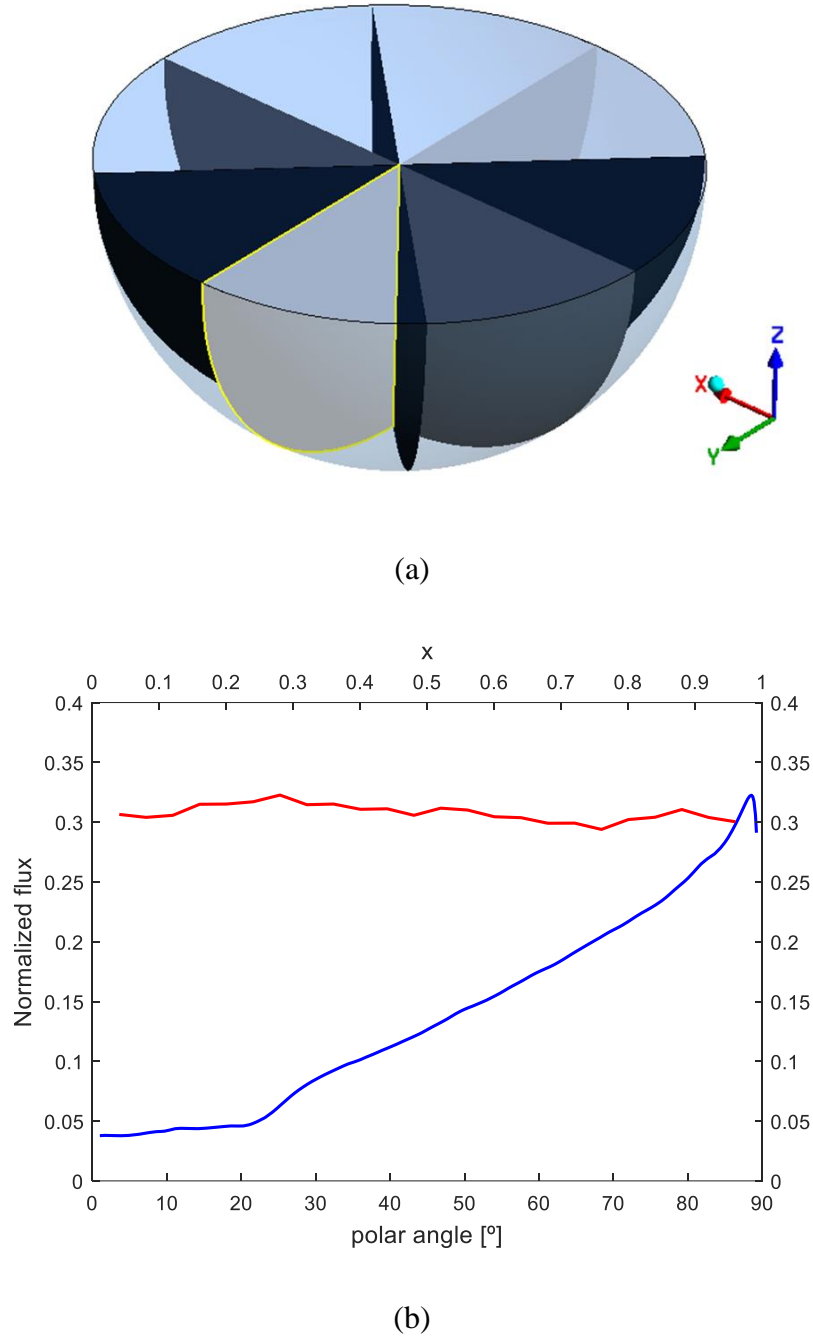

(a)

(b)

Figure 15 (a) 8 ¼ plane where the heat fluxes along the boundaries are averaged. (b)Heat flux profile along the boundaries of the middle slice. The red line is the heat flux along the top boundary, and the blue one is the heat flux along the curved boundary from the bottom (0 degree) to the top (90 degree).

4.4 TKE

The turbulent kinetic energy $k = \frac{1}{2}\left(\overline{u'u'} + \overline{v'v'} + \overline{w'w'}\right)$ can provide the intensity of the turbulence of the convective flow. It consists of three terms, $\overline{u'u'}$, $\overline{v'v'}$ and $\overline{w'w'}$, which represent the distribution on each velocity component. Figure 16 shows the mean TKE distribution. As indicated by the instantaneous velocity distribution of the flow, the energy is mainly located in the upper unstable zone and the descending flow, while it is relatively low in the stagnation area. Figure 17 provides the vertical plane-averaged profile (according to Figure 7(b)) of the root-mean-squared (rms) term of the fluctuation velocity in each direction, i.e., $\sqrt{\overline{u'u'}}$, $\sqrt{\overline{v'v'}}$ and $\sqrt{\overline{w'w'}}$. It shows that the vertical velocity rms $\sqrt{\overline{w'w'}}$ is significantly larger than the others in the upper part of the domain. In contrast, the horizontal velocity rms $\sqrt{\overline{u'u'}}$, $\sqrt{\overline{v'v'}}$ are much larger than the vertical one in the lower part. The reason for such a difference can be explained by looking at the contribution from the different budgets of TKE in the domain (Figure 18). For simplicity, only the budgets that are dominant are shown, namely, dissipation, production and buoyancy production, while the contribution of the remaining budgets is denoted as "others".

In the upper zone of the pool (z >0.5), the buoyancy production term in the TKE transport equation contributes to the energy dominantly, which means that the turbulence is mainly induced by the buoyancy force in the vertical direction. Thus, the TKE in the vertical direction term $\overline{w'w'}$ is much larger than the other ones. However, in the lower part of the domain, the buoyancy force suppresses the flow motion, so the buoyancy production of the TKE vanishes. Meanwhile, the normal production (shear production) of the TKE gradually increases and reaches its peak near the bottom, which indicates that the turbulence is mainly induced by the shear force caused by the descending flow. So, the horizontal terms of the TKE become larger than the vertical one in the lower domain.
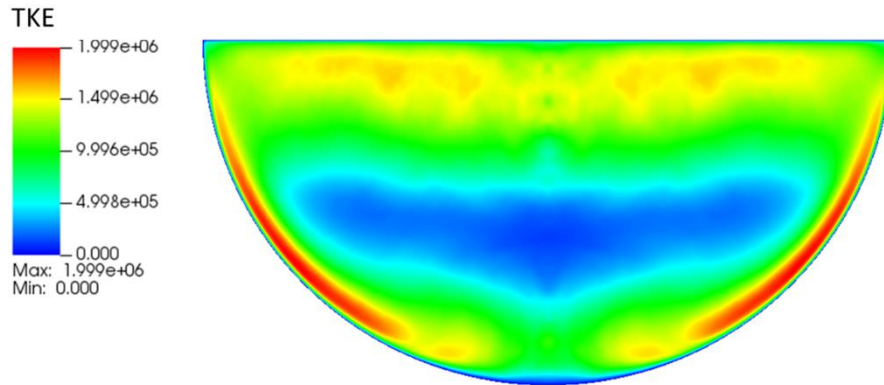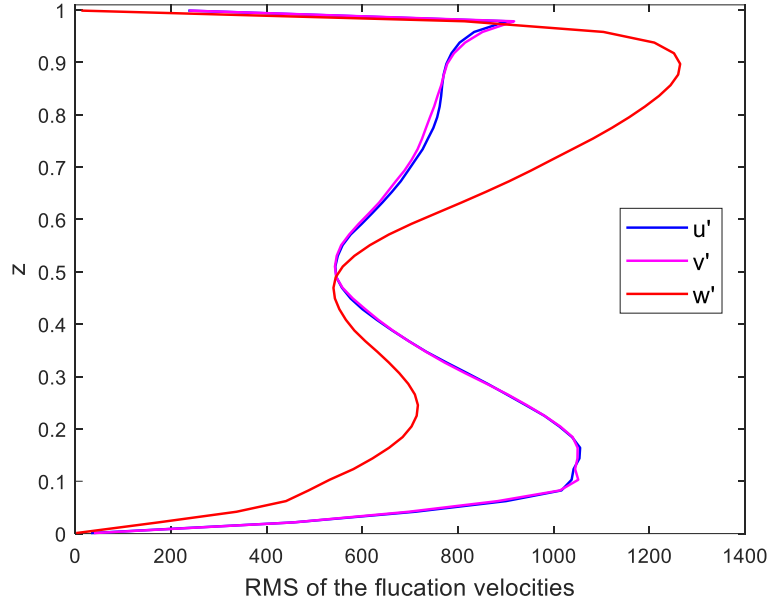

Figure 16 TKE distribution.

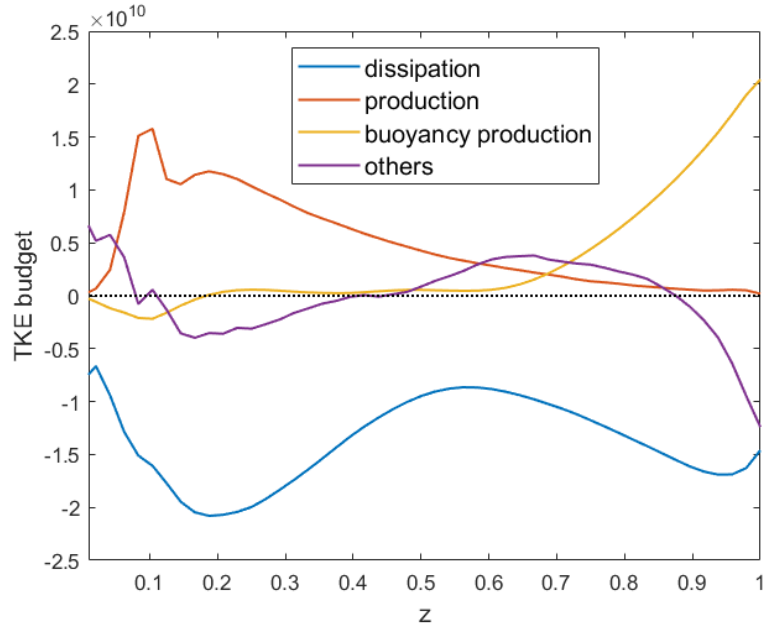Figure 17 RMS of the fluctuating velocity terms along the vertical planes.

Figure 18 TKE budgets along the vertical planes.

4.5 THF

In this part, we present for brevity only the results of the vertical THF, $\overline{w'\theta'}$, because it determines the buoyancy production of the TKE. The distribution of the other two THF terms can be found in the appendix. Figure 19 shows the distribution of $\overline{w'\theta'}$ on the middle slice of the domain. Its value is significantly higher near the boundaries in the upper zone of the domain.

In the upper unstable zone, where the flow is mainly prompted by the buoyancy force, the vertical THF $\overline{w'\theta'}$ is also relatively high. It can be explained by analysing its budgets (Figure 20). From the top to the bottom, the $\overline{w'\theta'}$ is mainly produced by the buoyancy production term. Near the top boundary, the buoyancy production and the shear production are balanced by the dissipation, the pressure temperature gradient and the turbulent diffusion. Near the bottom, the buoyancy is balanced by the shear production term.
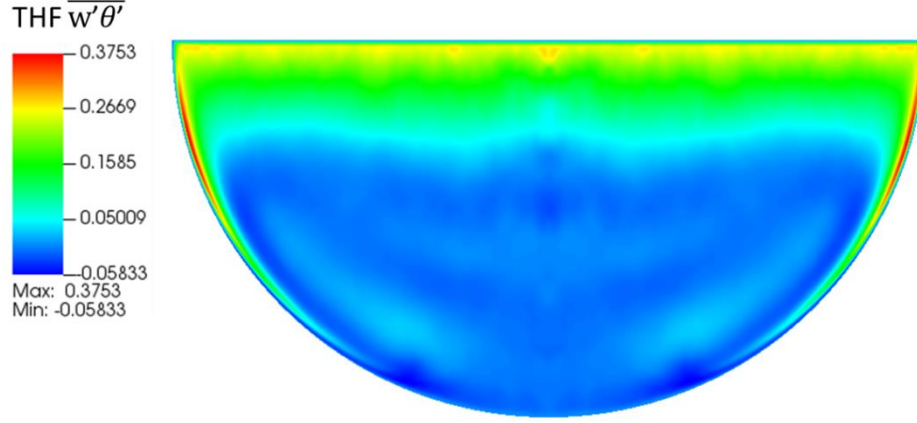

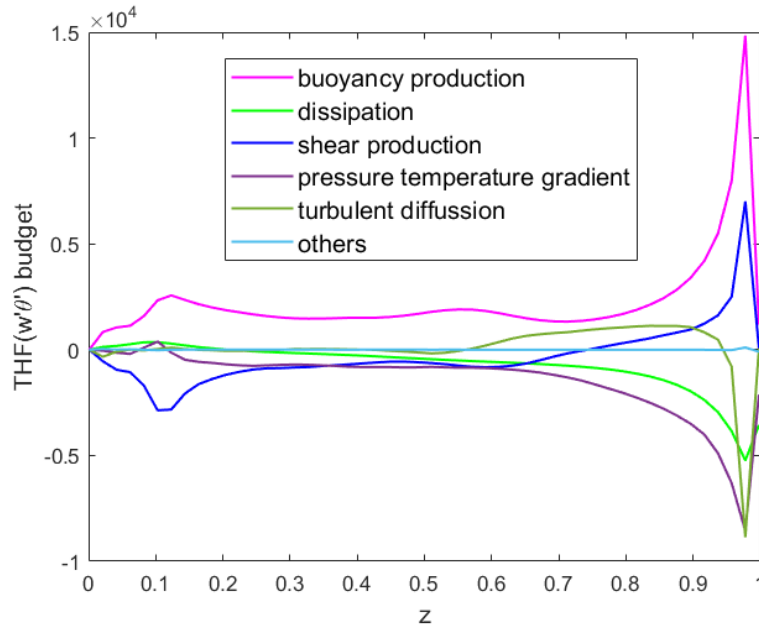Figure 19 Averaged turbulence heat flux distribution.

Figure 20 The budgets of the vertical turbulent heat flux $\overline{w'\theta'}$ along the vertical planes.

The buoyancy production of the vertical THF $\overline{w'\theta'}$ is an additional term that appears in case of buoyant flows, which is proportional to the variance of temperature, i.e., $B_{w'\theta'} = Ra\,Pr\cdot\overline{\theta'\theta'}$. Hence, it is essential to consider the temperature variance when modelling the turbulent heat flux in natural convection. For instance, in AHFM models, the temperature

variance is included in the algebraic expression of the turbulent heat flux, and an additional transport equation is utilized to close it. Here, we present the spatial averaged temperature variance distribution in Figure 21. It shows that $\overline{\theta'\theta'}$ is large along the top boundary where the buoyant effect is high, which is also reflected in the budget and the distribution of the $\overline{w'\theta'}$. Along the curved wall, it is also relatively high. Moreover, the high temperature variance along the curved wall also contributes to the production of the vertical THF $\overline{w'\theta'}$ there as shown in Figure 20.
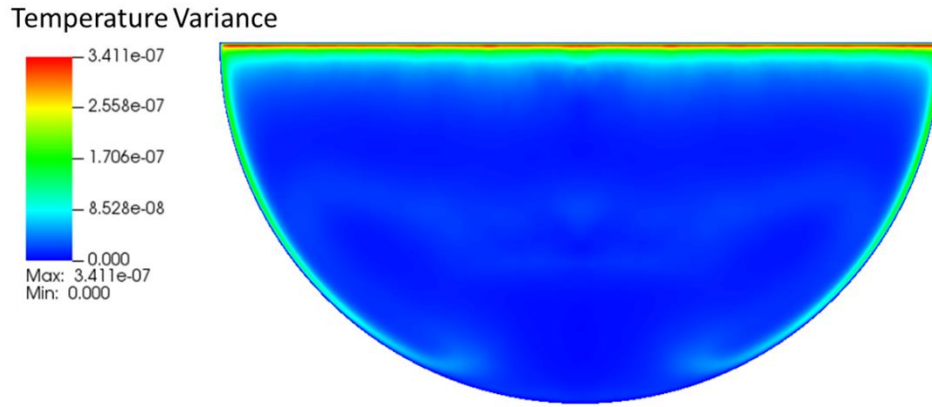

Figure 21 Temperature variance distribution.

5. Conclusions

In this study, a direct numerical simulation is conducted to investigate the behaviour of internally heated (IH) molten pool convection in a hemispherical domain at a Rayleigh number of 1.6×10^{11}. A reference Prandtl number Pr=0.5 is assumed, based on a prototypic corium material property. In agreement with the general observations from the BALI experiments, the thermo-fluid pattern in the volumetric heated pool can be divided into three distinct regions. First, the upper part features large turbulent eddies with cold plumes flowing down and wherein heat are effectively transported to top wall and nearby curved side wall. Second, the lower part features a nearly stagnant flow that is conducive for thermal stratification. Third, a descending flow can be observed along the curved wall that is responsible for transporting additional heat to the bottom, which also induces strong turbulence near the bottom. In addition, the heat flux distributions along the boundaries are investigated. Fluctuating heat fluxes are observed along the top boundary, which are caused by the turbulent eddies in the upper layer. Along the curved boundary, the heat flux increases nonlinearly as the polar angle (with reference zero polar angle at the bottom) and reaches its maximum value at the top.

Since intense turbulent flow is captured in the simulation, some detailed information of the turbulence is also presented in this work. The turbulent kinetic energy (TKE) distribution shows that the strongest turbulence occurs along the descending flow, and it is also strong in the upper unstable zone and the bottom area of the domain. From the budget analysis of TKE,

the turbulence energy is contributed by different mechanisms throughout the flow. In the upper unstable region, it is mainly induced by the buoyancy production effect, while it is mainly contributed by the shear production in the other regions. Further, the distribution and the budget of the vertical turbulent heat flux (THF) $\overline{w'\theta'}$ are given, since it is an important turbulent quantity for the modelling of the buoyancy production of the TKE. Finally, the temperature variance distribution $\overline{\theta'\theta'}$ is presented to provide the reference data, especially when modelling the turbulent heat fluxes in the RANS models.

An obvious extension of this work is to increase the Rayleigh number since it is still considered small compared to the prototypic values in the range of 10^{16}-10^{17}. But current capabilities of high-performance computing of supercomputers might render this range inaccessible. Nevertheless, a few orders of magnitude higher than the Ra=10^{11} considered here are still feasible [28]. In any case, the DNS data generated here can be used to assess LES and RANS models. Improved RANS models can then be used to run simulations with prototypic Ra numbers.

Funding

Competing Interests

On behalf of all authors, the corresponding author states that we have no known competing financial interests or personal relationships that could have appeared to influence the work reported in this paper.

Author Contributions

Boshen Bian: Conceptualization, Methodology, Calculation, Data curation, Visualization, Formal Analysis, Writing- Original draft preparation. Daniele Dovizio: Methodology, Writing- Reviewing and Editing. Walter Villanueva: Supervision, Conceptualization, Methodology, Writing- Reviewing and Editing, Funding and Computing Resources Acquisition.

References

1. Zhu, X., Mathai, V., Stevens, J.A.M., Verzicco, R., Lohse, D., "Reply: Comment, Phys. Rev. Lett. 123, 259401 (2019)," Phys. Rev. Lett. 123:259402, 2019.
2. Komlev, A., et al. (2019). Final report on stratified molten pool of simulant materials. EC-H2020 IVMR Project, No. 662157.
3. Bian, B., Villanueva, W., & Dovizio, D. (2022). Direct numerical simulation of molten pool convection in a 3D semicircular slice at different Prandtl numbers. Nuclear Engineering and Design, 393, 111772.
4. Goluskin, D. (2016). Internally Heated Convection and Rayleigh-Bénard Convection (1st ed. 2016. ed., Springer Briefs in Thermal Engineering and Applied Science).

5. Grossmann, S., & Lohse, D. (2000). Thermal Convection for Large Prandtl Numbers. Physical Review Letters 86, no. 15 (2001): 3316-319.

6. Goluskin, D. (2013). Zonal flow driven by convection and convection driven by internal heating.PhD Thesis, Columbia University.

7. Goluskin, David, & Van der Poel, Erwin P. (2016). Penetrative internally heated convection in two and three dimensions. Journal of Fluid Mechanics, 791, Journal of fluid mechanics, 2016-03-25, Vol.791.

8. Zhang, L., Zhou, Y., Zhang, Y., Tian, W., Qiu, S., & Su, G. (2015). Natural convection heat transfer in corium pools: A review work of experimental studies. Progress in Nuclear Energy (New Series), 79, 167-181.

9. Bernaz, L., Bonnet, J.M., Spindler, B., Villermaux, C. (1998). Thermal Hydraulic Phenomena in Cerium Pools: Numerical Simulation with TOLBIAC and Experimental Validation with BALI, OECD/CSNI Workshop on In-vessel Core Debris Retention and Coolability, Garching, Germany.

10. Kymäläinen, O, Tuomisto, H, Hongisto, O, & Theofanous, T.G. (1994). Heat flux distribution from a volumetrically heated pool with high Rayleigh number. Nuclear Engineering and Design, 149(1), 401-408.

11. Helle, M., Kymäläinen, O., Tuomisto, H. (1999). Experimental COPO II data on natural convection in homogenous and stratified pools. In: Proceedings of the Ninth International Topical Meeting on Nuclear Reactor Thermal-Hydraulics, NURETH-9, San Francisco, USA.

12. Sehgal, B.R., Bui, V.A., Dinh, T.N., Green, J.A., Kolb, G. (1998). SIMECO experiments on in-vessel melt pool formation and heat transfer with and without a metallic layer. In: Proc. OECD/CSNI Workshop, Garching, Germany.

13. Asfia, F.J, & Dhir, V.K. (1996). An experimental study of natural convection in a volumetrically heated spherical pool bounded on top with a rigid wall. Nuclear Engineering and Design, 163(3), 333-348.

14. Fluhrer, B., Alsmeyer, H., Cron, T., Messemer, G., Miassoedov, A., Wenz, T. (2005). The experimental programme LIVE to investigate in-vessel core melt behaviour in the late phase. In: Proc. of Jahrestagung Kerntechnik 2005, INFORUM GmbH, Nürnberg, Germany, pp. 198-201.

15. Zhang, Y.P, Zhang, L.T, Zhou, Y.K, Tian, W.X, Qiu, S.Z, Su, G.H, Ma, R.B. (2016). The COPRA experiments on the in-vessel melt pool behavior in the RPV lower head. Annals of Nuclear Energy, 89, 19-27.

16. Esmaili, H, & Khatib-Rahbar, M. (2005). Analysis of likelihood of lower head failure and ex-vessel fuel coolant interaction energetics for AP1000. Nuclear Engineering and Design, 235(15), 1583-1605.

17. Nourgaliev, R.R, Dinh, T.N, & Sehgal, B.R. (1997). Effect of fluid Prandtl number on heat transfer characteristics in internally heated liquid pools with Rayleigh numbers up to 1012. Nuclear Engineering and Design, 169(1-3), 165-184.

18. Shams, Afaque. (2018). Towards the accurate numerical prediction of thermal hydraulic phenomena in corium pools. Annals of Nuclear Energy, 117, 234-246.

19. Whang, Seokwon, Park, Hyun Sun, Lim, Kukhee, & Cho, Yong Jin. (2019). Prandtl number effect on thermal behavior in volumetrically heated pool in the high Rayleigh number region. Nuclear Engineering and Design, 351, 72-79.

20. Fukasawa, M., Hayakawa, S., & Saito, M. (2008). Thermal-hydraulic analysis for inversely stratified molten corium in lower vessel. Journal of Nuclear Science and Technology, 45(9), 873-888.

21. Zhang, L., Luo, S., Zhang, Y., Tian, W., Su, G., & Qiu, S. (2018). Large eddy simulation on turbulent heat transfer in reactor vessel lower head corium pools. Annals of Nuclear Energy, 111, 293-302.
22. Fregni, A., Angeli, D., Cimarelli, A., & Stalio, E. (2019). Direct numerical simulation of a buoyant triple jet at low-Prandtl number. International Journal of Heat and Mass Transfer , 143. doi: 10.1016/j.ijheatmasstransfer.2019.118466
23. Guo, W., & Prasser, H.-M. (2021). Mixed convection study on the influence of low Prandtl numbers and buoyancy in turbulent heat transfer using DNS. Annals of Nuclear Energy, 158. doi: 10.1016/j.anucene.2021.108258
24. Fischer, P. F., Lottes, J. W. & Kerkemeier, S. G. (2016), Nek5000 Web page. http://nek5000.mcs.anl.gov.
25. Patera, Anthony T. (1984). A spectral element method for fluid dynamics: Laminar flow in a channel expansion. Journal of Computational Physics, 54(3), 468-488.
26. Fischer, P., J. Lottes, S. Kerkemeier, O. Marin, K. Heisey, A. Obabko, E. Merzari, and Y. Peet. 2016. Nek5000: User's manual. Argonne National Laboratory.
27. Shishkina, Olga, Stevens, Richard J A M, Grossmann, Siegfried, & Lohse, Detlef. (2010). Boundary layer structure in turbulent thermal convection and its consequences for the required numerical resolution. New Journal of Physics, 12(7), 075022.
28. Bian, B., Gong, J., & Villanueva, W. (2022). Scalability of Nek5000 on High-Performance Computing Clusters Toward Direct Numerical Simulation of Molten Pool Convection. Frontiers in Energy Research, 10. https://doi.org/10.3389/fenrg.2022.864821